Combined Impact of Asymmetric Critical Current and Flux Diverters on AC Loss of a 6.5 MVA/25 kV HTS Traction Transformer

Yue Wu, Wenjuan Song, *Member, IEEE*, Stuart C. Wimbush, *Senior Member, IEEE*, Jin Fang, Rodney A. Badcock, *Senior Member, IEEE*, Nicholas J. Long, and Zhenan Jiang, *Senior Member, IEEE*

***Abstract*—A 6.5 MVA/25 kV high temperature superconducting (HTS) transformer for the Chinese Fuxing high-speed train has been proposed to replace the oil-based transformers while achieving higher efficiency, lighter weight, and minimized volume. The high targeted efficiency (> 99%) makes AC loss reduction a vital issue. HTS coated conductors generally exhibit asymmetric critical current characteristics as a function of magnetic field angle $I_c(B, \theta)$, leading to a non-trivial influence on the AC loss of coil windings. The fast-computing *T-A* homogenization method is proposed to calculate the AC loss of the 6.5 MVA/25 kV traction transformer with large turn numbers. The variables, *T* and *A*, are the current and magnetic vector potentials, respectively. The AC loss of the transformer windings is analyzed for various coil configurations with and without flux diverters considering $I_c(B, \theta)$. At the rated current and 65 K, employing the flux diverters with a square-shape cross-section, the total AC loss is decreased by 73.7% and an extra 150 W loss reduction was also obtained. Moreover, an additional reduction of 37 W is realized upon utilizing the asymmetric $I_c(B, \theta)$ characteristic. The reduced 187 W in AC loss at 65 K corresponds to a reduction in ambient power requirement of over 5.6 kW. Therefore, considering asymmetric $I_c(B, \theta)$, can lead to a non-trivial reduction in AC loss, even incorporating flux diverters.**

***Index Terms*—AC Loss, asymmetric critical current, flux diverters, HTS traction transformer, *T-A* homogenization method.**

This work was partially supported by the Chinese Ministry of Science and Technology through the National Key Research and Development Program of China under Grant No. 2016YFE0201200. This work was also supported in part by the New Zealand Ministry of Business, Innovation and Employment under Contract No. RTVU1707 and in part by the Strategic Science Investment Fund "Advanced Energy Technology Platforms" under Contract No. RTVU2004. *(Corresponding author: Zhenan Jiang and Jin Fang).*

Y. Wu and J. Fang are with the School of Electrical Engineering, Beijing Jiaotong University, Beijing, 100044, China (e-mail: yue.wu@vuw.ac.nz; jfang@bjtu.edu.cn).

W. Song is with the James Watt School of Engineering, The University of Glasgow, Glasgow G12 8QQ, United Kingdom (e-mail: wenjuan.song@glasgow.ac.uk).

S. C. Wimbush, R. A. Badcock, N. J. Long and Z. Jiang are with the Robinson Research Institute, Victoria University of Wellington, 69 Gracefield Road, Lower Hutt 5011, New Zealand (e-mail: stuart.wimbush@vuw.ac.nz; rod.badcock@vuw.ac.nz; nick.long@vuw.ac.nz; zhenan.jiang@vuw.ac.nz).

Color versions of one or more of the figures in this article are available online at http://ieeexplore.ieee.org

NOMENCLATURE

Abbreviations

DPC	Double-pancake coil.
HTS	High temperature superconducting.
REBCO	$REBa_2Cu_3O_{7-x}$, rare-earth barium-copper-oxide (high-temperature superconductors).
HV	High voltage.
LV	Low voltage.
T-A	The current vector potential and the magnetic vector potential.

Parameters

B_{axial}, B_z	Axial magnetic field component [T].
B_{radial}, B_r	Radial magnetic field component [T].
B_0	Characteristic magnetic field [T].
I_c	Critical current [A].
J_{c0}	Self-field critical current density [A/m^2].
J_{bulk}	Calculated current density in the homogeneous bulk [A/m^2].
n	Power index of the superconductor.
α	Exponent of field dependence of critical current.
ρ_{HTS}	Resistivity of the superconductor [Ω·m].

Variables

A	Magnetic vector potential [T·m].
B	Magnetic flux density [T].
J	Current density [A/m^2].
T	Current vector potential [A/m].
θ	Angle between the normal to the conductor face and the magnetic field direction in a left-handed system with respect to the direction of current flow [deg].

Functions

$I_c(B, \theta)$	Critical current as a function of different magnitudes and relative orientations of the applied magnetic field [A].
$J_c(B)$	Critical current density as a function of the magnetic field [A/m^2].

I. Introduction

TO meet growing expectations for the electrification of transportation, high-speed trains with high energy-efficiency and large passenger capacity undoubtedly will play a major role in mass transportation. As one of the most critical components of high-speed trains, HTS (high temperature superconducting) traction transformers for advanced transportation technology offer many advantages over conventional copper-based transformers such as high efficiency, light weight, and low fire hazard [1]-[5]. There has been an ongoing international project targeting the Chinese Fuxing high-speed trains led by Beijing Jiaotong University partnered with the Robinson Research Institute of Victoria University of Wellington to develop a single-phase 6.5 MVA/25 kV HTS traction transformer [6]. The goal of the project is to achieve a transformer system having a weight less than 3 tons, better than 99% efficiency, and 43% short-circuit impedance [6]. From previous experience of HTS transformers, the design and operation of transformer systems are challenged by the difficulty of extracting the heat produced by AC loss while considering the cooling penalty in the cryogenic environment [5]. Reducing AC loss is recognized as one of critical issues in the project to achieve the efficiency and weight target.

Recent decades have witnessed the rapid development of (RE)$Ba_2Cu_3O_{7-x}$ (REBCO) coated conductors, with many successful demonstrations of HTS technologies such as transformers [7]-[16], rotating machines [17]-[21], power transmission cables [22]-[25], and fault current limiters [26]-[32] using these conductors. However, REBCO conductors present asymmetric critical current characteristics $I_c(B, \theta)$ under magnetic fields B applied in different directions θ, due to their planar structure and the microstructural flux pinning centers intentionally introduced during the production process [33] (Fig. 1). This asymmetric characteristic has a non-trivial influence on both the critical current and the AC loss of isolated conductors and coil windings [34]-[40]. Recently, the asymmetric $I_c(B, \theta)$ characteristics of the coated conductors have been used to estimate AC loss in the coil windings of the Robinson 1 MVA transformer [41]. A 15% AC loss reduction was obtained by simply flipping the direction of the top and bottom halves of the coil windings of the 1 MVA transformer in order to take advantage of this asymmetry, providing a novel approach to reducing AC loss in the 6.5 MVA/25 kV traction transformer [41].

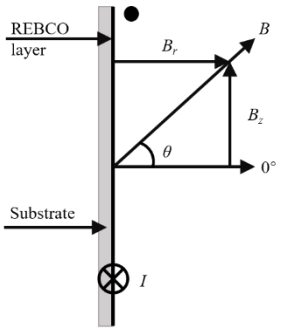

Fig. 1. Schematic of field angle θ with respect to the HTS conductor. θ is defined as the angle between the normal to the conductor face and the magnetic field direction in a left-handed system with respect to the direction of current flow.

Previous studies have shown numerically that the AC loss of a 6.5 MVA/25 kV traction transformer with ≥ 1 m winding length, constructed using high-performance HTS wires, can be reduced below 2.0 kW by positioning flux diverters at the ends of the coil windings [42]-[47]. The role of the flux diverters is to reduce the AC loss in the HTS coil windings by shaping the magnetic field around the coils [48]-[49]. Utilizing the asymmetric $I_c(B, \theta)$ behavior of REBCO wires has the potential to further reduce the AC loss and system weight [41] as well as increasing the efficiency of the transformer. Therefore, it is important to investigate the combined impact of the asymmetric $I_c(B, \theta)$ characteristics of REBCO wires and flux diverters on the AC loss of the 6.5 MVA/25 kV traction transformer.

A schematic of the 6.5 MVA/25 kV traction transformer is shown in Fig. 2. The gap between the two transformer units shown in the figure causes an asymmetric magnetic field distribution in the end and middle sections of the transformer windings. The quarter model used in earlier simulations is inadequate to capture this asymmetric magnetic field distribution [50] and a half model has to be used to investigate the impact of the asymmetric $I_c(B, \theta)$ behavior on the AC loss of the traction transformer. The total turn number of the transformer exceeds ten thousand turns and hence the *H* formulation is incapable of dealing with such a large turn number due to excessive computation time [51]-[53]. In contrast, the *T-A* formulation treats the thin HTS coated conductors as 1D lines without any thickness and hence reduces the required number of mesh elements thereby speeding up the computation [54]-[55]. The homogenization method where stacks of superconductors are treated as blocks ignoring actual sample dimensions can significantly reduce the computing time without compromising the accuracy of the simulation result [56]-[57]. There have been some studies on simulations of HTS coils using *T-A* formulation combined with the homogenization method to speed up the computing time [58]. However, there has been no report on simulations for HTS transformers. To summarize, the contributions of this paper are outlined as follows:

1) Encompassing real-world modelling of HTS devices, for the first time, the *T-A* homogenization method is applied to the 6.5 MVA/25 kV HTS traction transformer, validating its capability and providing an efficient way to deal with large-scale HTS applications.

2) The combined impact of both the asymmetric $I_c(B, \theta)$ characteristics of HTS coated conductors and flux diverters is investigated for the first time to further reduce AC loss in the 6.5 MVA/25 kV HTS traction transformer which in turn can improve the efficiency and reduce the system weight of the transformer.

3) We demonstrate a substantial AC loss reduction in the 6.5 MVA traction transformer achieved through a simple, cost-neutral procedure (flipping the coils) that is unique to HTS windings.

In this work, we carried out 2D *T-A* homogenization method AC loss studies on a 6.5 MVA/25 kV HTS traction transformer giving consideration to the combination of the asymmetric critical current of HTS wires and the use of flux diverters to shape the field. Section II presents critical equations for the *T-A* formulation and the homogenization method. To validate the numerical method,

Section III compares experimental AC loss results of the Robinson 1 MVA transformer [50] with those obtained through the new simulation. Based on the different winding structures of the high voltage (HV) and low voltage (LV) windings, Section IV illustrates the engineering feasibility of exploiting the critical current asymmetry in each case. Then, considering the measured $I_c(B, \theta)$ characteristics of exemplary coated conductors, AC loss simulations of the 6.5 MVA/25 kV traction transformer with various coil configurations and with or without flux diverters are presented and the simulated current density distributions, magnetic field distributions around the transformer coils and AC loss results compared.

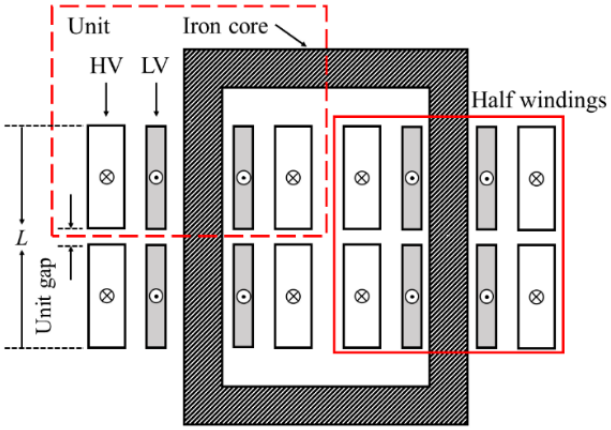

Fig. 2. Schematic of the 6.5 MVA/25 kV traction transformer. The quarter model indicated by the broken red line is inadequate to capture the asymmetric field distribution, so a half model indicated by the solid red line was used. The direction of current flow in each of the windings is indicated by the dot and cross symbols.

II. Numerical Method

In this section, the *T-A* formulation and the homogenization method are described.

A. T-A Formulation

The current vector potential $\boldsymbol{T}$ is applied to the superconducting region and the magnetic vector potential $\boldsymbol{A}$ is used in the non-superconducting region. $\boldsymbol{T}$ and $\boldsymbol{A}$ can be expressed in terms of the current density $\boldsymbol{J}$ and the magnetic flux density $\boldsymbol{B}$ as:

$$\boldsymbol{J} = \nabla \times \boldsymbol{T} \tag{1}$$

$$\boldsymbol{B} = \nabla \times \boldsymbol{A} \tag{2}$$

The governing equations of the $\boldsymbol{T}$ formulation and the $\boldsymbol{A}$ formulation are:

$$\nabla \times \left(\frac{1}{\mu_0 \mu_r} \nabla \times \boldsymbol{A} \right) = \boldsymbol{J} \tag{3}$$

$$\nabla \times \left(\rho_{HTS} \nabla \times \boldsymbol{T} \right) = -\frac{\partial \boldsymbol{B}}{\partial t} \tag{4}$$

where μ_0 is the vacuum permeability, μ_r is the relative permeability, and ρ_{HTS} is the resistivity of the superconductor given by the *E*-*J* power law:

$$\rho_{HTS} = \frac{E_c}{J_c(\boldsymbol{B})} \left| \frac{\boldsymbol{J}}{J_c(\boldsymbol{B})} \right|^{n-1} \tag{5}$$

where $E_c = 10^{-4}$ V/m and n is the power index. In order to validate the numerical method used in this work by making a fair comparison with previous simulation results, n values and $J_c(B)$ equations for the 1 MVA transformer are consistent with published works [50]. Thus, the n value is set to 30 for the 1 MVA transformer. For the 6.5 MVA/25 kV traction transformer, the n value is assumed to be 25 and $J_c(B, \theta)$ curves are derived from the measured $I_c(B, \theta)$ data divided by the cross-section of the HTS layer.

The transport current in the superconducting tapes is calculated by integrating the current density $\boldsymbol{J}$:

$$I = \iint_S \boldsymbol{J} \mathrm{d}S = \iint_S \nabla \times \boldsymbol{T} \mathrm{d}S = \oint_{\partial S} \boldsymbol{T} \mathrm{d}l \tag{6}$$

where S is the cross section of the conductor.

As shown in Fig. 3, since $\boldsymbol{T}$ is defined to be normal to the tape surface, the transport current for a single tape is:

$$I = (T_1 - T_2) \cdot d \tag{7}$$

where T_1 and T_2 are the values of $\boldsymbol{T}$ on the top and bottom edges, and d is the thickness of the HTS layer (assumed to be 1 μm).

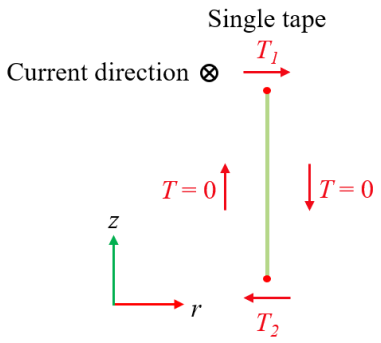

Fig. 3. Boundary conditions of the transport current for a single tape.

B. T-A Homogenization Method

The *T-A* homogenization method was introduced in [54] and was shown to be efficient in dealing with large scale HTS devices assembled from thousands of turns of HTS wire. This efficient method is used to approximate coil windings in this work. Under this method, turns in the coil having similar electromagnetic properties are treated as a bulk, as depicted in Fig. 4.

In the 2D *T-A* homogenization model, T_1 and T_2 are the values of $\boldsymbol{T}$ on boundaries at the top and bottom edges of equivalent homogeneous bulks.

The calculated current density in the homogeneous bulk defined for the $\boldsymbol{A}$ formulation is:

$$\boldsymbol{J}_{bulk} = \boldsymbol{J} \cdot \frac{d}{t} \tag{8}$$

where t is the thickness of the whole HTS wire, including the copper stabilizer, silver overlayer, HTS layer, buffer stack and substrate [59].

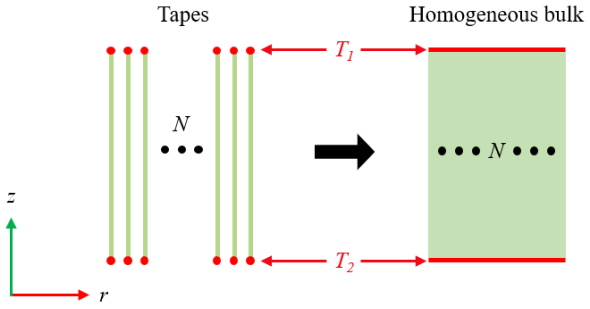

Fig. 4. Homogenization method for the 2D *T-A* model. The superconducting tapes are transformed into a homogeneous bulk. The boundary conditions T_1 and T_2 are applied to the edges corresponding with the extreme points of the tapes.

III. Model Validation

To validate the *T-A* homogenization method, AC loss simulation results of the Robinson 1 MVA transformer [50] are compared with their experimental results. In addition, the computing time of the *H* and *T-A* homogenization methods is estimated at different normalized currents to verify the superiority of the *T-A* homogenization method. All numerical simulations were carried out using 2D FEM (finite element method) models [60]-[63] implemented in COMSOL Multiphysics [64]-[67].

For the 1 MVA transformer, the HV windings comprise 24 double-pancake coils (DPCs) per phase wound with 4 mm wide SuperPower REBCO wires, while the LV windings utilize 20-turn single-layer solenoid windings per phase wound with fully transposed 15/5 Roebel cables (fifteen 5 mm wide strands) made from SuperPower tapes [68]. Table I lists the specifications of the 1 MVA transformer.

TABLE I

Specifications of the 1 MVA Transformer

Specification	HV winding	LV winding
Inner diameter	345 mm	310 mm
Turn number in axial direction	48	20
Turn number in radial direction	19	1
Total number of turns	912	20
Conductor width	4 mm	12.1 mm
Conductor thickness	0.22 mm	0.8 mm
Axial gap between turns	2.13 mm	2.1 mm
Roebel strand number	-	15
Roebel strand width	-	5 mm
Gap between Roebel stacks	-	2.1 mm
Constant I_c used in the model	118.7 A	2226 A
Rated current amplitude	42.9 A	1964 A

In comparison with the AC loss results obtained via the *H* homogenization method presented in [50], the $J_c(B)$ dependence keeps consistent with the following equation [69]:

$$J_c(B) = J_{c0}\left(1+\frac{|B_{radial}|}{B_0}\right)^{-\alpha} \tag{9}$$

where B_{radial} is the radial magnetic field in the two-dimensional axisymmetric model, J_{c0} is the self-field critical current density, B_0 and α are fitting parameters obtained from critical current measurement under applied magnetic fields. These magnetic field dependence parameters used in the HV and LV windings are listed in Table II.

TABLE II

MAGNETIC FIELD DEPENDENCE PARAMETERS OF THE 1 MVA TRANSFORMER

Parameter	HV winding	LV winding
J_{c0}	2.12×10^{10} A/m^2	3.55×10^{10} A/m^2
B_0	149 mT	149 mT
α	0.6	0.6

Fig. 5 shows the structured meshes for the upper end of the 1 MVA transformer. It is worth emphasizing that the 15/5 Roebel cable is equivalent to two parallel stacks, with each stack containing eight strands [70]-[71] In the radial direction, the LV windings and HV windings are divided into 4 and 8 sub-blocks, respectively. In the axial direction, finer meshes are used in the end part of the coil windings with 50 elements in the LV windings and 40 elements in the HV windings, since the larger radial magnetic field generated at the end part of coil windings contributes most of the ac loss. For the middle part of the windings, coarser meshes are used with 25 elements in the LV windings and 20 elements in the HV windings. Moreover, the diameter of the semicircular air domain is set to 10 times larger than the outer diameter of the HV winding, and the fine free triangular mesh is applied to the remaining air domain.

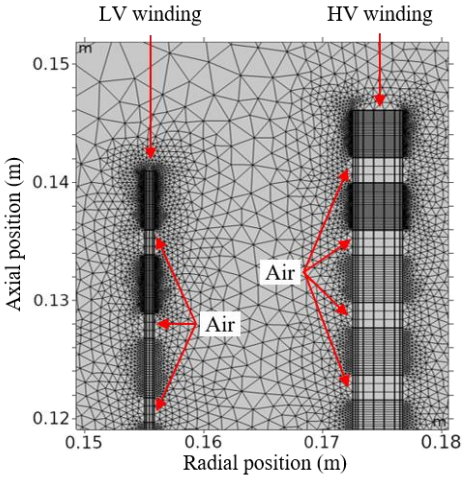

Fig. 5. Structured meshes for the upper end of the 1 MVA transformer.

Fig. 6 shows the magnetic flux density distribution and flux lines at the end of the coil windings at rated current, f = 50 Hz, and t = 3/4 cycle (the negative peak of one period). The area between the LV and HV windings experiences the stronger magnetic flux density. Flux lines are more perpendicular to the face of the HTS conductor in the end turns of the coil windings implying greater AC loss in this region.

Fig. 7 shows the normalized current density distribution within the end coils of the LV and HV windings. The high current density ($|J/J_c|>1$) region of the disc closer to the end of the winding is likely to be larger than the neighboring one, which indicates a higher AC loss.

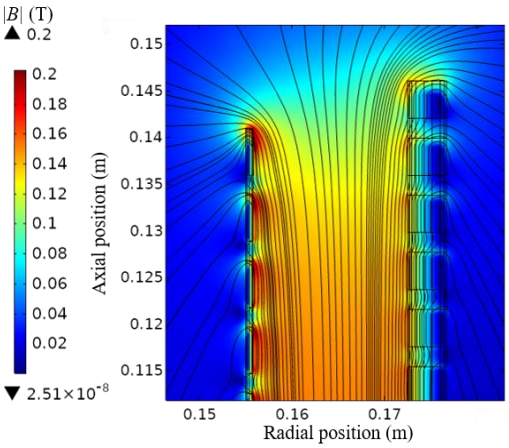

Fig. 6. Magnetic flux density distribution and flux lines towards the end of the 1 MVA transformer at rated current (f = 50 Hz, t = 3/4 cycle).

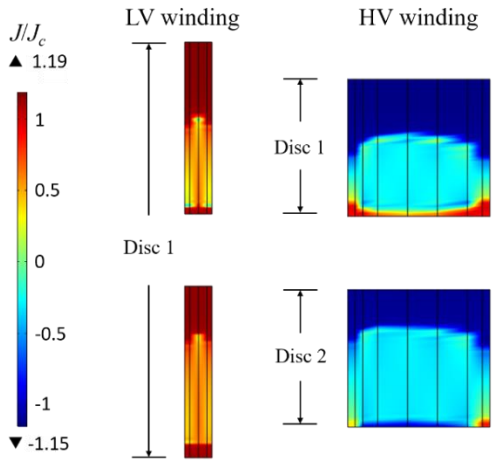

Fig. 7. Normalized current density distribution within the end coils of the LV and HV windings of the 1 MVA transformer at rated current (f = 50 Hz, t = 3/4 cycle).

In Fig. 8, assuming a short-circuited secondary winding, the AC loss, including eddy current loss per phase of the 1 MVA transformer calculated by the *T-A* formulation is compared with values obtained using the *H* formulation [50] and acquired by measurement [68]. Considering the eddy current loss caused by the solid copper terminal blocks at the ends of the LV winding, the measured AC loss is 112.3 W at I_{rated} = 1964 A and f = 50 Hz. The numerical results at rated current simulated using the *T-A* formulation and the *H* formulation are 87.5 W and 67.1 W, respectively. The calculated AC loss values utilizing the *T-A* formulation provide a better agreement with experimental results at different transport currents than the *H* formulation.

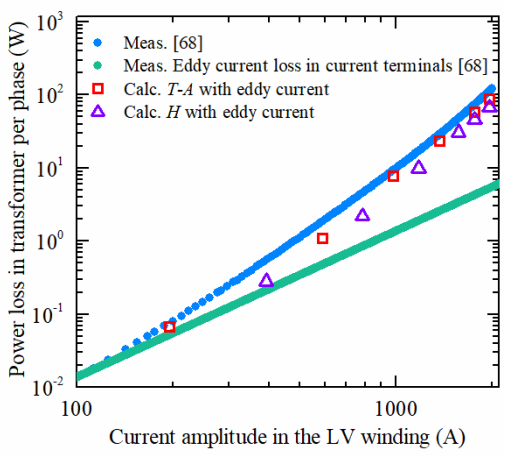

Fig. 8. Calculated AC loss in the 1 MVA transformer compared with measured results. The Meas. eddy current loss [68] is the eddy current loss in the current terminals of the LV winding, and the Meas. [68] is the summation of the winding loss and the Meas. eddy current loss [68].

Table III presents the computation time at different normalized currents using the *H* and *T-A* homogenization methods on an Intel Xeon W-2135 processor, 3.70 GHz, and 64 GB RAM. All simulation models of the 1 MVA transformer have the same structured meshes with Ref. [50] for a fair comparison. At I/I_{rated} = 0.3 and 1, the *T-A* homogenization method is 10 times and 5 times faster than the *H* homogenization method clearly demonstrating its advantage over the *H* homogenization method both in accuracy and computing time.

TABLE III

COMPARISON OF THE COMPUTATION TIME BETWEEN THE *H* AND *T-A* HOMOGENIZATION METHODS IN 2D FOR THE 1 MVA TRANSFORMER.

Normalized current (I/I_{rated})	Computation time	
	H homogenization method	*T-A* homogenization method
0.3	3.12 h	0.29 h
0.5	3.22 h	0.33 h
0.7	3.34 h	0.47 h
1	3.47 h	0.61 h

IV. SIMULATION RESULTS AND DISCUSSION

As depicted in Fig. 2, the basic design for the 6.5 MVA/ 25 kV transformer has four units, each unit has one HV winding and one LV winding, and two units are located around each leg of the iron core. The HV windings are wound with HTS coated conductors, whereas the LV windings are wound with 8/5 Roebel cables (eight 5 mm wide strands). More detailed specifications are listed in Table IV. The HV windings employ stacks of DPCs, and the LV windings are multi-layer solenoid windings. Each turn of 8/5 Roebel cable in the LV winding is simulated as two parallel stacks, each with four conductors carrying the same current in each conductor [6].

The AC loss is considered as the winding loss, excluding the core loss generated by the iron core for simplicity. To prevent the heat from hysteretic loss in the iron core imposing a large load on the cryogenic cooling system, the iron core is located outside the cryostat. In addition, due to the relatively large distance between the core and windings (30 mm) compared to oil-based transformers and its very high permeability (21220 at 1.6 T), the magnetic iron core should have a minor impact on the winding loss [68].

TABLE IV

SPECIFICATIONS OF THE 6.5 MVA/25 KV TRACTION TRANSFORMER

Specification	Value
Winding length L	1 m
Number of turns in each HV winding disc	14
Number of discs stacked to make the HV winding per unit	116
Number of layers of 8-strand Roebel cable in LV winding	3
Number of turns in one layer in LV winding	40
Total number of turns per unit in HV winding	1624
Total number of turns per unit in LV winding	120
Inner diameter of HV winding	437 mm
Inner diameter of LV winding	285 mm
Axial gap between the two units on each leg of the core	20 mm
Short-circuit impedance	43%
Rated current amplitude in HV winding	90.9 A
Rated current amplitude in LV winding	1196.4 A
Short-circuit voltage	10.75 kV

A. AC Loss Exploiting Measured $I_c(B, \theta)$

Since high-performance Fujikura wires are used in the design of the 6.5 MVA/25 kV HTS traction transformer [6], and it presents a symmetric $I_c(B, \theta)$ characteristic, in order to investigate the influence of $I_c(B, \theta)$ asymmetry on AC loss in this work, the HTS wires used in the HV winding and the assembled Roebel cable in the LV winding were all modelled as SuperPower SCS4050-AP wires. As shown in Fig. 9, this type of SuperPower conductor displays a highly asymmetric $I_c(B, \theta)$ characteristic under applied magnetic field [41], having a significantly different I_c at $\pm \theta$, and when the field is reversed from θ to $180°-\theta$. For fair AC loss analysis, the measured $I_c(B, \theta)$ of the SuperPower wire (Fig. 9) was scaled by a constant factor to take the 65 K self-field I_c from 693.3 A/cm to 1140 A/cm to match that of the high-performance Fujikura wire [6].

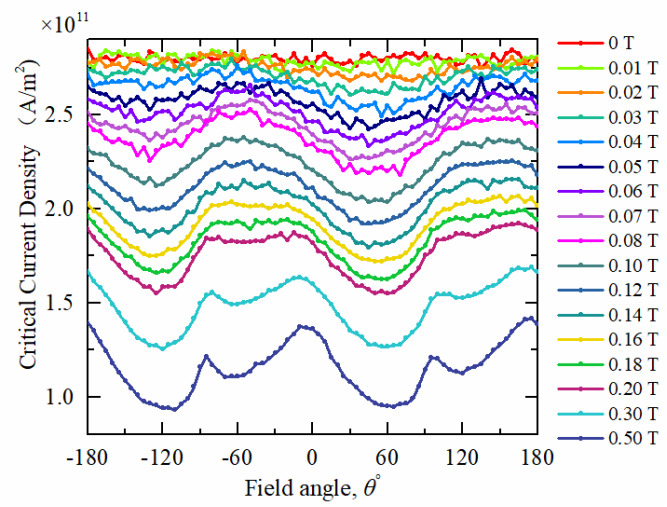

Fig. 9. Measured $I_c(B, \theta)$ dependences of the SuperPower SCS4050-AP wire at 65 K [41].

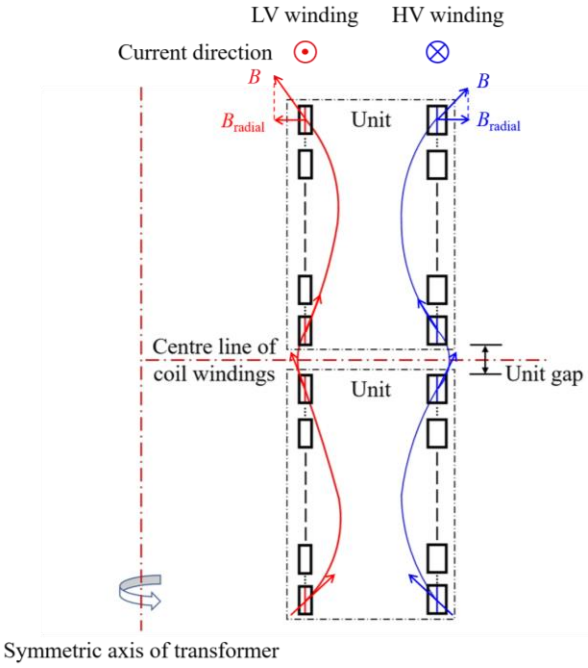

Fig. 10. Schematic of the magnetic field distribution on the right side of the transformer windings.

Fig. 10 depicts a schematic of the magnetic field distribution on the right side of the transformer windings. In operation, the currents in the HV and LV windings have opposite signs so that the resulting magnetic fields also have opposite directions. Furthermore, the radial (perpendicular) magnetic field component in the top and bottom units is greater than that in the middle part of the transformer windings.

As shown in Fig. 11, the coil windings are classified as the top winding, the top-middle winding, the bottom-middle winding, and the bottom winding depending on their relative position along the *z*-axis. Regarding the $I_c(B, \theta)$ dependence, the different coil

orientations of the HV and LV windings are defined as follows: the reference coil orientation is denoted as U, and the field angle relative to the coil is θ. When the coil is flipped, its orientation is denoted as L, and the field angle is inverted and offset by 180°.

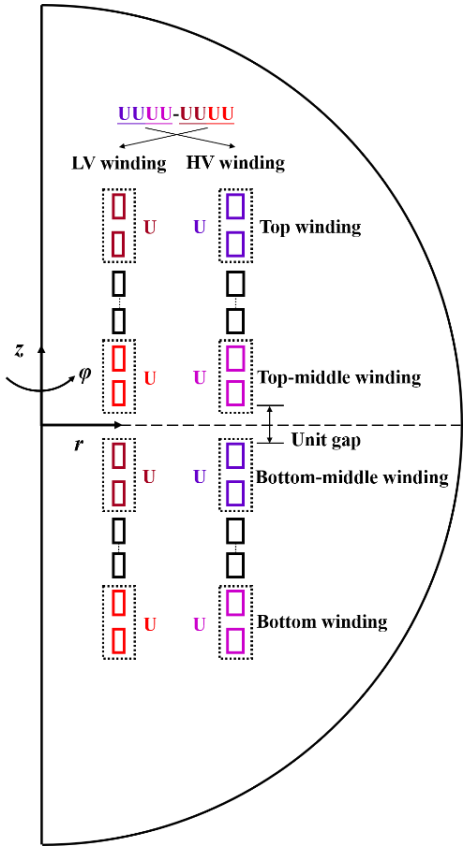

Fig. 11. Definition of the coil configurations. The actual diameter of the semicircular air domain for simulation is set to 10 times larger than the outer diameter of the HV winding.

Fig. 12 shows the schematic of flipping the DPCs in the HV windings. It is worth emphasizing that this is a simple and cost-neutral procedure during transformer assembly. In the case of the LV windings, taking advantage of the anisotropy of the conductor is more difficult, since these constitute a single full-length solenoid wound from Roebel cable. Inverting the wire in the upper half therefore requires a cut to be made in the cable (at point A′B on the left side of Fig. 13) followed by re-splicing (to form the joint AB on the right side of the figure). Given the difficulty of manufacturing long-length coated conductors, an LV winding without splicing is not practical, so this doesn't introduce an additional processing step, again therefore presenting a feasible modification to the standard assembly process. One practical approach to consider is to punch pre-spliced coated conductors in the production of the strands for the Roebel cable.

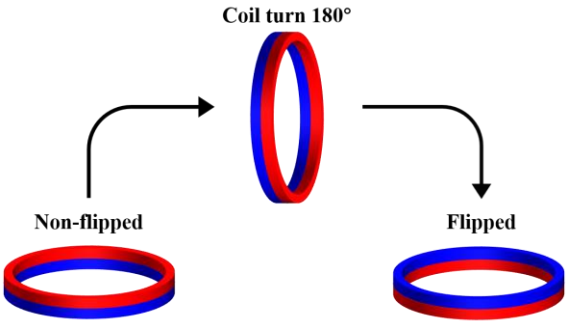

Fig. 12. Schematic drawing of the flipping of a double pancake coil.

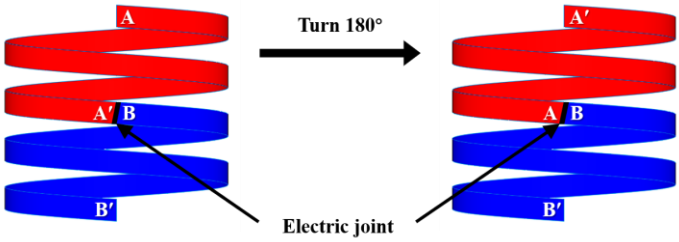

Fig. 13. Schematic drawing of the flipping of the upper half of one layer in the solenoid winding. AA′ and BB′ are spliced Roebel strands before assembling.

When taking both the HV and LV windings into account, each winding requires four characters to describe its coil orientations, so together eight characters are required. For example, in the case UUUU-UUUU, the first four characters denote the coil orientations of the HV winding, while the last four characters denote the coil orientations of the LV winding. As indicated in Fig. 11, each character corresponds to a different position of the winding from top to bottom.

Although the LV winding has a helical solenoid structure, it is simplified as a series of disc windings in the axisymmetric model. Two discs in the LV winding are equivalent to one turn of Roebel cable. At the unit level, 8 DPCs of the HV winding and 16 discs of the LV winding, in the top and top-middle windings, or in the bottom-middle and bottom windings, are flipped in the simulation model to investigate the AC loss effected by the $I_c(B, \theta)$ behavior. Since most AC loss is generated at the end part of the transformer windings, the dashed rectangles highlighted in Fig. 11 show the location of these selected coils.

It is a huge task to consider all 256 possible combinations of coils in the HV and LV windings. In this work, only six representative configurations are evaluated: UUUU-UUUU, LLLL-UUUU, LLUU-LLUU, UULL-UULL, UUUU-LLLL, and LLLL-LLLL.

Fig. 14 shows the magnetic field angle in the different parts of the HV and LV windings before and after flipping. In the case of the top part of the HV winding, the field angle is defined as α before flipping, then flipping the coil causes the field angle to become $180°-\alpha$. In the case of the top part of the LV winding, due to the opposite direction of the current flow, the field angle is defined as $-\beta$ before flipping, and the field angle becomes $180°+\beta$ after flipping the coil. Since the top-middle and bottom-middle windings have different magnetic field distributions than the top and bottom windings, α' and β' are used to describe the differences in the field angles.

α' and β' are slightly smaller than α and β due to the magnetic cancellation. In the other cases, the definitions of the magnetic field angles before and after flipping follow the same principle.

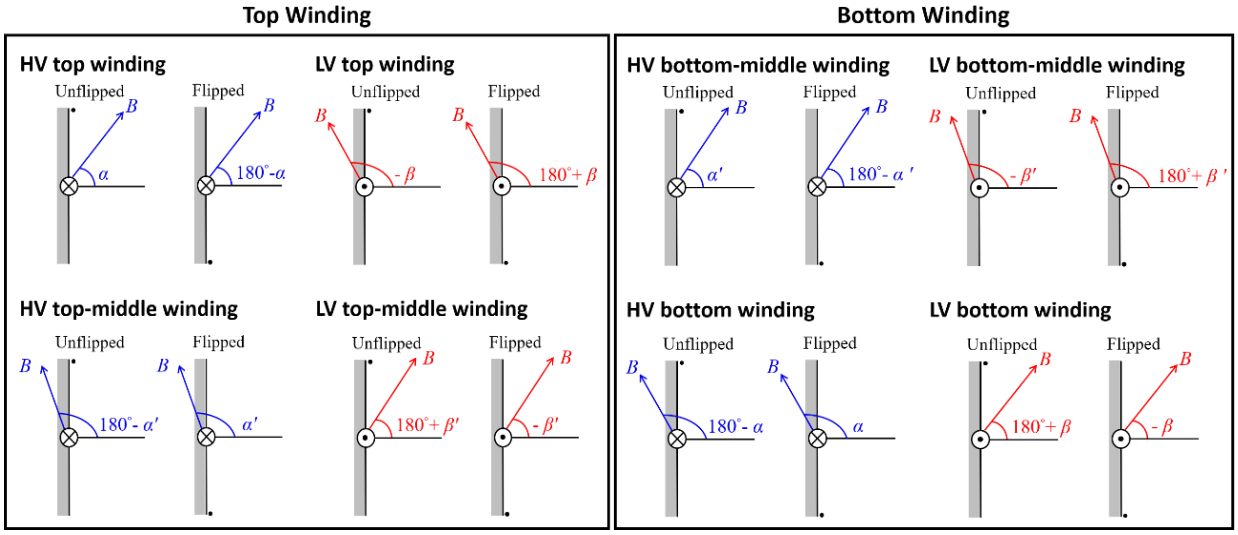

Fig. 14. Definition of the coil orientation in the LV and HV windings before and after flipping.

In the simulation model, a three-column look-up table [B_{radial}, B_{axial}, $J_c(B_{radial}, B_{axial})$] is formulated, where B_{radial} and B_{axial} are the radial and axial components of the local magnetic field, and $J_c(B_{radial}, B_{axial})$ is the critical current density calculated from the measured $I_c(B, \theta)$ curves divided by the cross-sectional area of the HTS layer.

We explain the magnetic field components determined from the field angle combined with Fig. 14, taking the top part of the HV and LV windings as an example. In the top part of the HV winding, before flipping the coil, $B_{radial} = B\cos(\alpha) = B_r$, $B_{axial} = B\sin(\alpha) = B_z$, then upon flipping the coil, $B_{radial} = B\cos(180°-\alpha) = -B_r$, $B_{axial} = B\sin(180°-\alpha) = B_z$. In the top part of the LV winding, before flipping the coil, $B_{radial} = B\cos(-\beta) = B_r$, $B_{axial} = B\sin(-\beta) = -B_z$, then upon flipping the coil, $B_{radial} = B\cos(180°+\beta) = -B_r$, $B_{axial} = B\sin(180°+\beta) = -B_z$. B_r' and B_z' are likewise used to represent the magnetic field components in the top-middle and bottom-middle windings. Tables V and VI list all the B_{radial} and B_{axial} components of the HV and LV windings at the different winding positions for the different configurations.

TABLE V

MAGNETIC FIELD COMPONENTS DETERMINED FROM THE FIELD ANGLES OF THE HV WINDING

	UUUU-UUUU	LLLL-UUUU	LLUU-LLUU	UULL-UULL	UUUU-LLLL	LLLL-LLLL
Top winding	(B_r, B_z)	($-B_r$, B_z)	($-B_r$, B_z)	(B_r, B_z)	(B_r, B_z)	($-B_r$, B_z)
Top-middle winding	($-B_r'$, B_z')	(B_r', B_z')	(B_r', B_z')	($-B_r'$, B_z')	($-B_r'$, B_z')	(B_r', B_z')
Bottom-middle winding	(B_r', B_z')	($-B_r'$, B_z')	(B_r', B_z')	($-B_r'$, B_z')	(B_r', B_z')	($-B_r'$, B_z')
Bottom winding	($-B_r$, B_z)	(B_r, B_z)	($-B_r$, B_z)	(B_r, B_z)	($-B_r$, B_z)	(B_r, B_z)

TABLE VI

MAGNETIC FIELD COMPONENTS DETERMINED FROM THE FIELD ANGLES OF THE LV WINDING

	UUUU-UUUU	LLLL-UUUU	LLUU-LLUU	UULL-UULL	UUUU-LLLL	LLLL-LLLL
Top winding	(B_r, $-B_z$)	(B_r, $-B_z$)	($-B_r$, $-B_z$)	(B_r, $-B_z$)	($-B_r$, $-B_z$)	($-B_r$, $-B_z$)
Top-middle winding	($-B_r'$, $-B_z'$)	($-B_r'$, $-B_z'$)	(B_r', $-B_z'$)	($-B_r'$, $-B_z'$)	(B_r', $-B_z'$)	(B_r', $-B_z'$)
Bottom-middle winding	(B_r', $-B_z'$)	(B_r', $-B_z'$)	(B_r', $-B_z'$)	($-B_r'$, $-B_z'$)	($-B_r'$, $-B_z'$)	($-B_r'$, $-B_z'$)
Bottom winding	($-B_r$, $-B_z$)	($-B_r$, $-B_z$)	($-B_r$, $-B_z$)	(B_r, $-B_z$)	(B_r, $-B_z$)	(B_r, $-B_z$)

Fig. 15 presents the radial magnetic field distribution and magnetic flux lines of the UUUU-UUUU configuration. The two Roebel coils in the top part of the LV winding (Fig. 15 (a)) experience a larger radial magnetic field than those in the top-middle part (Fig. 15 (c)), owing to the cancellation of magnetic field that occurs in the gap between the transformer units. The same conclusion can be drawn from Fig. 15 (b) and Fig. 15 (d) for the HV winding.

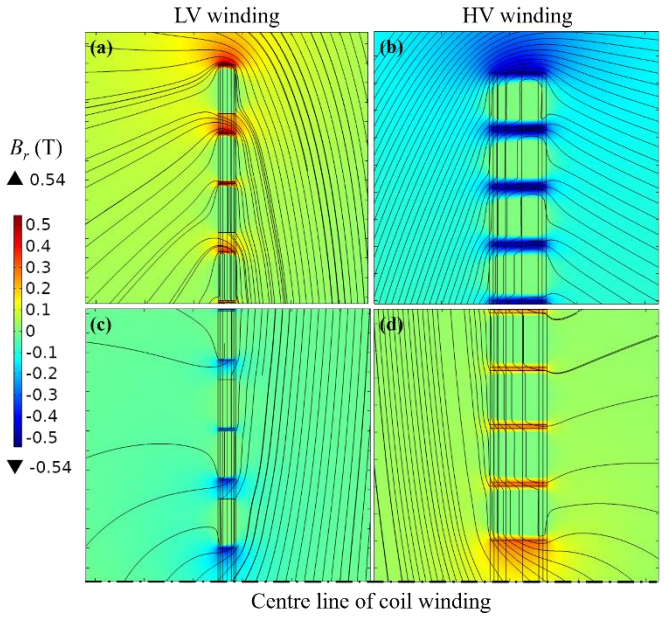

Fig. 15. The radial magnetic field distribution and magnetic flux lines of the UUUU-UUUU configuration in the 6.5 MVA/25 kV transformer: (a) Top part of the LV winding; (b) Top part of the HV winding; (c) Top-middle part of the LV winding; (d) Top-middle part of the HV winding.

Table VII lists the AC loss simulation results for each coil configuration. For the initial coil configuration, UUUU-UUUU, calculated AC loss values of the HV and LV windings are 3089.8 and 809.6 W; most AC loss is generated by the HV winding. The LLLL-UUUU configuration corresponds to flipping 16 DPCs of the HV winding, while the UUUU-LLLL configuration corresponds to flipping 32 discs of the LV winding. Flipping the HV winding reduces the AC loss by 32.6 W, while flipping the LV winding only reduces it by 19.1 W. Then 8 DPCs and 16 discs in the top half and bottom half of the HV and LV windings are flipped, embodied in the LLUU-LLUU and UULL-UULL configurations. The AC loss reductions obtained by these two coil configurations are very close,

20.1 and 25.7 W, respectively. Finally, entirely flipping all 16 DPCs of the HV winding and 32 discs of the LV winding, the LLLL-LLLL configuration, gives the most pronounced AC loss reduction of 51.0 W, 34.3 W in the HV winding and 16.7 W in the LV winding. If estimating the reduction with a cooling penalty factor of 30 at 65 K [68], at least 1.5 kW can be saved for the onboard cooling system. It is also worth noting that this significant (>1%) reduction in AC loss is achieved simply by reversing the coil orientation in the transformer windings.

Fig. 16 compares the normalized current density distribution in the HV and LV windings for the UUUU-UUUU and LLLL-LLLL configurations. In general, the LLLL-LLLL configuration exhibits less $|J/J_c|>1$ area than the UUUU-UUUU configuration. The difference is slight, but tracing along the dashed lines superimposed on the images, it can be seen that the $|J/J_c|>1$ area in the UUUU-UUUU configuration crosses the lines, compared with the LLLL-LLLL configuration where it does not. As for the HV winding, the region where $|J/J_c|>1$ is larger than in the LV windings, which corresponds with the simulation results showing that the AC loss mostly originates from the HV winding. Making a comparative analysis of the top and top-middle parts of the HV and LV windings, the top winding has a greater $|J/J_c|>1$ area, implying a large proportion of the AC loss is generated at the end part of the transformer windings.

TABLE VII

SIMULATED AC LOSS RESULTS FOR THE 6.5 MVA/25 KV TRACTION TRANSFORMER UNDER DIFFERENT COIL CONFIGURATIONS

Configuration	HV winding	LV winding	Total	Difference to UUUU-UUUU	
UUUU-UUUU	3089.8 W	809.6 W	3.90 kW	-	-
LLLL-UUUU	3056.3 W	810.5 W	3.87 kW	32.6 W	0.84%
LLUU-LLUU	3078.0 W	801.3 W	3.88 kW	20.1 W	0.52%
UULL-UULL	3072.6 W	801.1 W	3.87 kW	25.7 W	0.66%
UUUU-LLLL	3088.3 W	792.0 W	3.88 kW	19.1 W	0.49%
LLLL-LLLL	3055.5 W	792.9 W	3.85 kW	51.0 W	1.32%

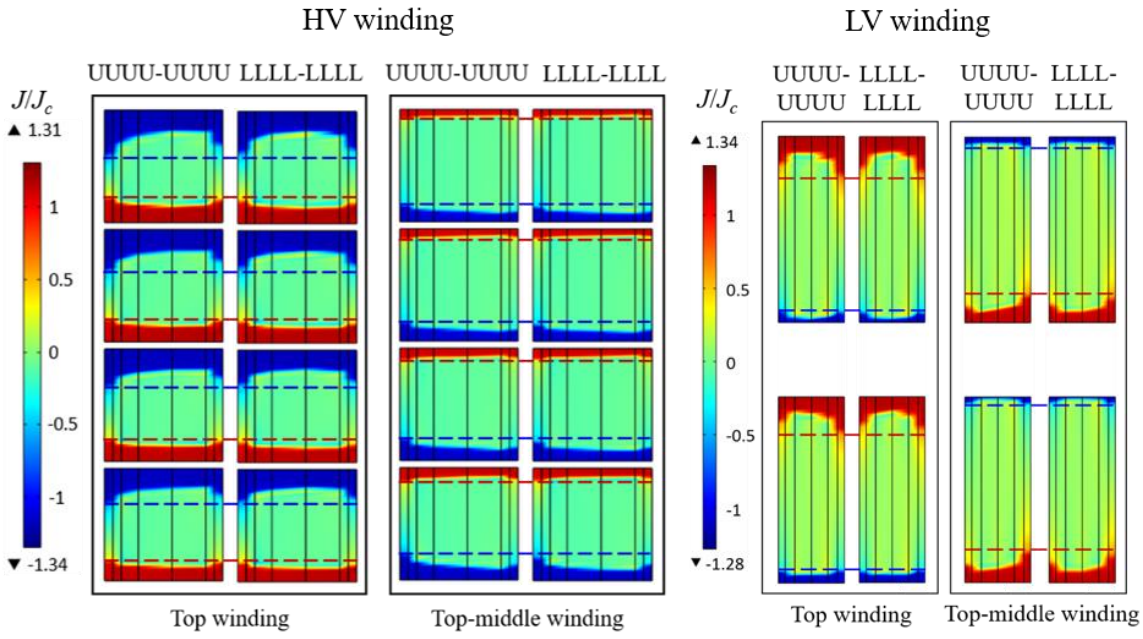

Fig. 16. Comparison of the normalized current density distribution in the HV and LV windings at the rated current for the UUUU-UUUU and LLLL-LLLL configurations: (a) the HV winding; (b) the LV winding.

B. AC Loss Combining $I_c(B, \theta)$ and Flux Diverters

Previous sections have observed that a substantial AC loss reduction is possible in transformer windings through flipping the coil orientation. In the following, to further improve the efficiency of the 6.5 MVA/25 kV transformer and reduce the overall weight of the cooling system [72], AC loss investigations utilizing the flipping method together with the application of flux diverters are conducted.

Fig. 17 depicts the arrangement of flux diverters positioned near the ends of the LV and HV windings. As shown in Table VIII, FD1 with a rectangular shape and FD2 with a square shape were designed for exploring their influence on AC loss. The dimensions of the flux diverters for the LV winding are expressed as $W_{\mathrm{FD,\,LV}}$ and $H_{\mathrm{FD,\,LV}}$, while $W_{\mathrm{FD,\,HV}}$ and $H_{\mathrm{FD,\,HV}}$ denote the dimensions of the flux diverters for the HV winding. W_{E} indicates the overhanging distance to the inner radius of the LV and HV windings, and g represents the distance between the end of the LV or HV winding and the flux diverter. The flux diverters are considered to be made of a compressed powder ferromagnetic material with a nominal relative permittivity μ_{r} of 100.

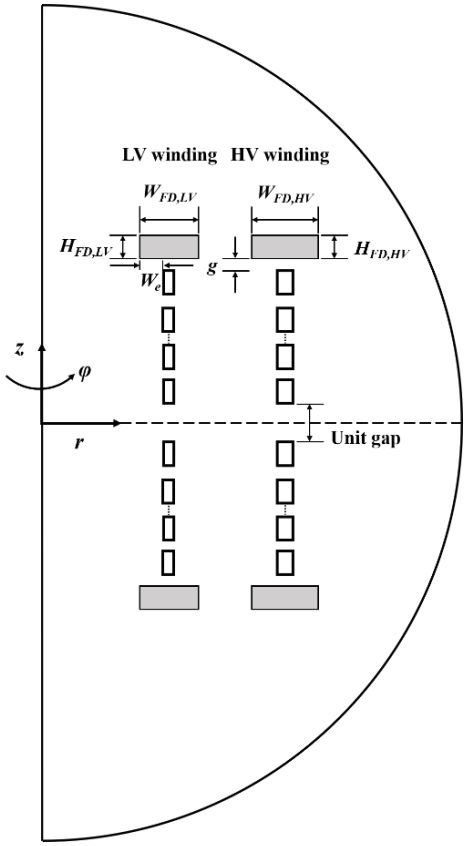

Fig. 17. Schematic showing the position and dimensions of flux diverters located at the ends of the windings.

TABLE VIII

DIMENSIONS OF FLUX DIVERTERS

Parameter	FD1	FD2
W_E	8 mm	8 mm
g	0.5 mm	0.5 mm
$W_{FD,\,LV}$	17.8 mm	17.8 mm
$H_{FD,\,LV}$	3.8 mm	17.8 mm
$W_{FD,\,HV}$	20.2 mm	20.2 mm
$H_{FD,\,HV}$	6.2 mm	20.2 mm

Fig. 18 shows the radial magnetic field distribution and magnetic flux lines of the UUUU-UUUU configuration with flux diverter FD1 at the rated current. Comparing with Fig. 15 without flux diverters, the flux lines in the windings become more parallel to the coil surface in the presence of the flux diverters. The maximum radial field component decreases from 0.54 T to 0.13 T with flux diverters for the top coil in the LV winding, and from 0.52 T to 0.19 T for the top coil in the HV winding. The high magnetic permeability of the flux diverters results in magnetic field concentration, reshaping the magnetic flux distribution around the windings to reduce the perpendicular magnetic field component of the coil winding and thereby reduce the AC loss.

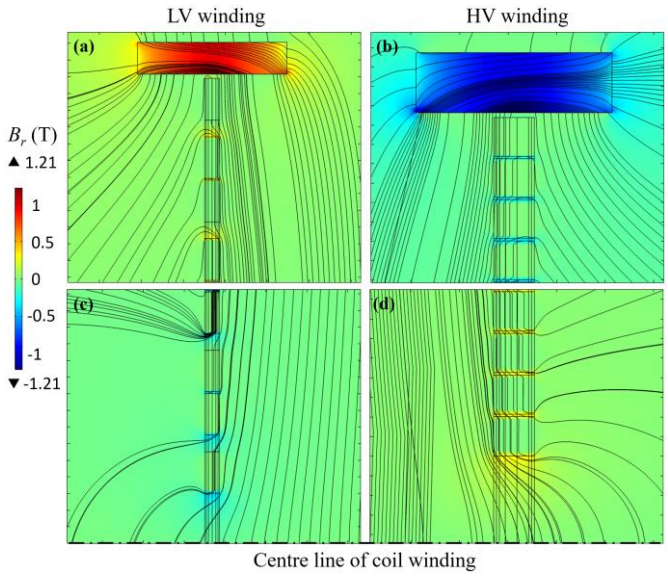

Fig. 18. The radial magnetic field distribution and magnetic flux lines of the UUUU-UUUU configuration in the 6.5 MVA/25 kV transformer with flux diverter FD1 at the rated current: (a) Top part of the LV winding; (b) Top part of the HV winding; (c) Top-middle part of the LV winding; (d) Top-middle part of the HV winding.

Table IX gives the simulated AC loss for each coil configuration at the rated current coupled with flux diverter FD1. For the UUUU-UUUU configuration, the total AC loss is 3.90 kW without flux diverters, but just 1.95 kW with flux diverters. This result reveals that positioning flux diverters at the end of the coil windings greatly reduces the AC loss. Compared with the UUUU-UUUU configuration, the LLLL-LLLL configuration obtains the further reduction in AC loss is 37.1 W, or almost 2%, indicating that flipping makes coils find their optimal orientation with a larger critical current density and reduce AC loss. The LLLL-LLLL configuration remains the optimized choice of these possible coil configurations. Thus, flipping coils at the end of transformer windings is still a valid AC loss reduction technique even in the presence of flux diverters.

TABLE IX

SIMULATED AC LOSS RESULTS FOR THE 6.5 MVA/25 KV TRACTION TRANSFORMER COUPLED WITH FLUX DIVERTERS FD1

Configuration	HV winding	LV winding	Total	Difference to UUUU-UUUU	
UUUU-UUUU	1579.8 W	366.7 W	1.95 kW	-	-
LLLL-UUUU	1563.1 W	367.8 W	1.93 kW	15.6 W	0.80%
LLUU-LLUU	1571.7 W	356.5 W	1.93 kW	18.3 W	0.94%
UULL-UULL	1571.7 W	356.4 W	1.93 kW	18.4 W	0.95%
UUUU-LLLL	1580.0 W	346.2 W	1.93 kW	20.3 W	1.05%
LLLL-LLLL	1563.0 W	346.4 W	1.91 kW	37.1 W	1.92%

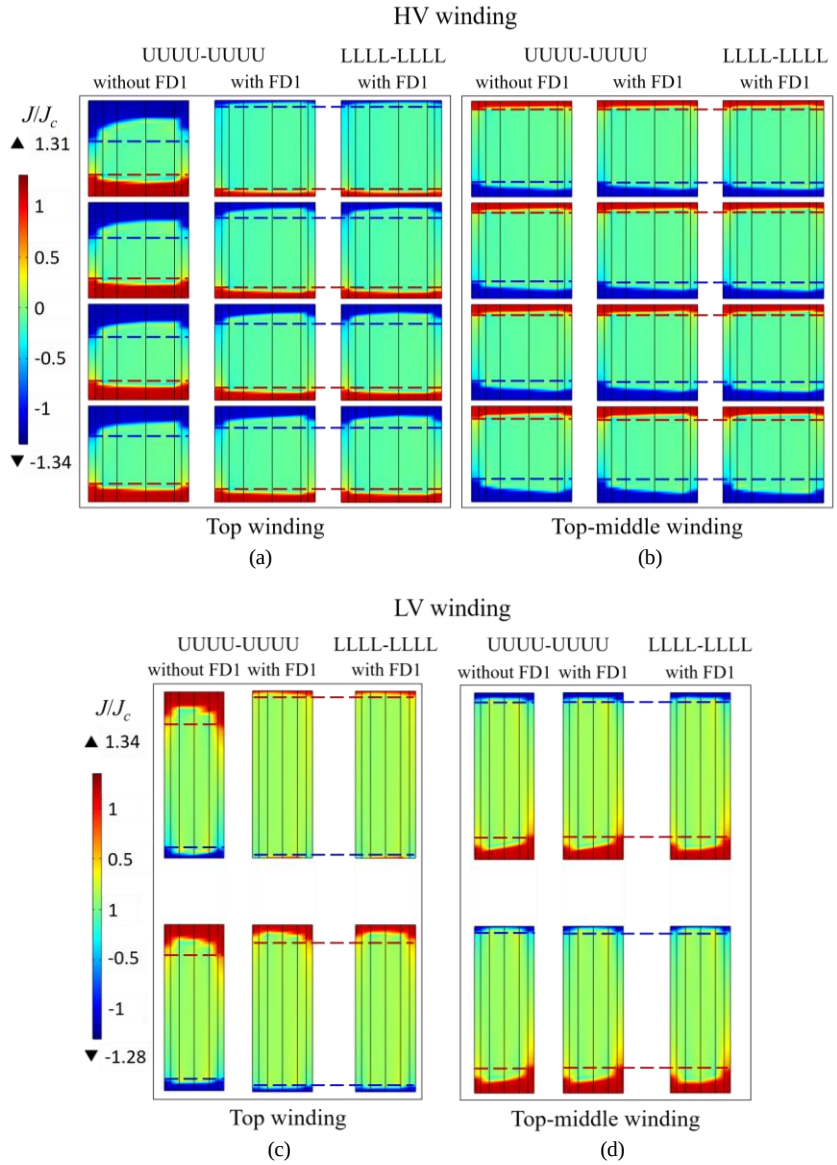

Fig. 19. Comparison of the normalized current density distribution in the HV and LV windings at the rated current with flux diverter FD1 for the UUUU-UUUU and LLLL-LLLL configurations: (a) Top part of the HV winding; (b) Top-middle part of the HV winding; (c) Top part of the LV winding; (b) Top-middle part of the LV winding.

Fig. 19 compares the normalized current density distribution in the HV and LV windings with flux diverter FD1 for the UUUU-UUUU and LLLL-LLLL configurations. The $|J/J_c|>1$ area in the coil windings with flux diverters is smaller than that without flux diverters. Moreover, compared to the UUUU-UUUU configuration, the $|J/J_c|>1$ region further decreases in the LLLL-LLLL configuration. For Fig. 19 (a) and (c), combining with Fig. 18, top parts of the HV and LV windings, coils at this position are next to FDs, flux lines are parallel to the coil surface, significantly reducing fully penetrated areas where $|J/J_c|>1$, and leads to valuable loss reduction. Curiously, as shown in Fig. 19 (c), the shielding current disappears in the disc closest to FDs, proving there is almost no perpendicular magnetic field in this disc, as presented in Fig. 18. For the top-middle windings situated far from the flux diverters, it

can be seen that the flux diverters have almost no effect on AC loss because the $|J/J_c|>1$ region in the UUUU-UUUU configuration is almost the same with or without flux diverters. Nevertheless, this region also decreases in the LLLL-LLLL configuration showing that the AC loss reduction is mainly caused by flipping when the coils are situated some distance from the flux diverters. The results indicate the asymmetric $I_c(B, \theta)$ characteristic continues to contribute to AC loss reduction, which gives the opportunity to further decrease AC loss also in the presence of flux diverters.

Table X gives the simulated AC loss for each coil configuration at the rated current coupled with flux diverter FD2. For the UUUU-UUUU configuration, the total AC loss of the 6.5 MVA/25 kV traction transformer is significantly reduced to 1.80 kW. Since the square-shaped FD2 has a larger cross-section, the AC loss becomes smaller when compared with the AC loss result coupled with FD1. For the LLLL-LLLL configuration, an additional 36.7 W reduction in AC loss is achieved through flipping the coil orientation. These results imply that both the dimensions of the flux diverters and an optimized coil configuration play an important role in AC loss reduction.

TABLE X

SIMULATED AC LOSS RESULTS FOR THE 6.5 MVA/25 KV TRACTION TRANSFORMER COUPLED WITH FLUX DIVERTERS FD2

Configuration	HV winding	LV winding	Total	Difference to UUUU-UUUU	
UUUU-UUUU	1442.9 W	357.4 W	1.80 kW	-	-
LLLL-UUUU	1426.5 W	357.6 W	1.78 kW	16.2 W	0.90%
LLUU-LLUU	1434.9 W	347.1 W	1.78 kW	18.3 W	1.02%
UULL-UULL	1440.2 W	347.2 W	1.79 kW	12.9 W	0.72%
UUUU-LLLL	1443.4 W	336.8 W	1.78 kW	20.1 W	1.12%
LLLL-LLLL	1426.6 W	337.0 W	1.76 kW	36.7 W	2.06%

Fig. 20 shows the difference between the AC loss values in the UUUU-UUUU and LLLL-LLLL configurations with and without flux diverters. Even at different currents, the LLLL-LLLL configuration remains the best option to reduce AC loss, which indicates the $I_c(B, \theta)$ asymmetry has a significant influence on the AC loss through adjusting coil orientation. Meanwhile, the square-shaped flux diverter FD2 with a larger cross-sectional area is seen to have a better capability to suppress the AC loss than the rectangular-shaped FD1.

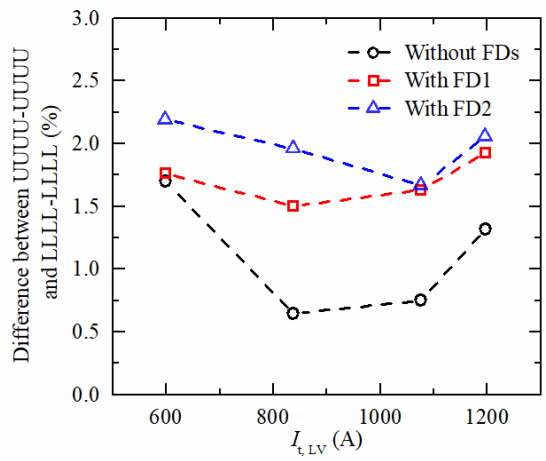

Fig. 20. Comparison of the difference between AC loss values in UUUU-UUUU and LLLL-LLLL configurations with and without flux diverters.

Fig. 21 shows absolute AC loss values in the UUUU-UUUU and LLLL-LLLL configurations with both flux diverters FD1 and FD2. The AC loss values of the UUUU-UUUU configuration with FD1 and FD2 are 1.95 and 1.80 kW, respectively: increasing the cross-sectional area of the flux diverters directly results in 150 W of AC loss reduction at 65 K, equivalent to 4.5 kW saving at room temperature. In addition, the LLLL-LLLL configuration leads to the same conclusion. Comparing the UUUU-UUUU and LLLL-LLLL configurations, an additional loss reduction is obtained. This figure reiterates the conclusions, once again, that a substantial AC loss reduction was obtained when exploiting the $I_c(B, \theta)$ asymmetry and using flux diverters with a larger cross-section.

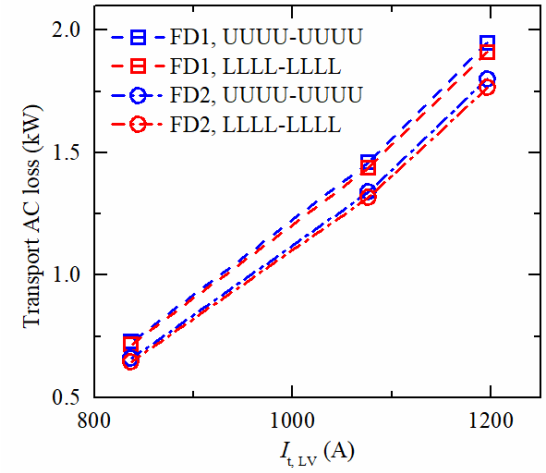

Fig. 21. Comparison of AC loss values in the UUUU-UUUU and LLLL-LLLL configurations with the FD1 and FD2.

V. Conclusion

In this work, for first time, we proposed the use of a *T-A* homogenization method to simulate AC loss in a 6.5 MVA/25 kV HTS traction transformer considering the combined impact of both the asymmetric $I_c(B, \theta)$ characteristics of HTS coated conductors and

the use of flux diverters to shape the field. The *T-A* homogenization method offers a 5 – 10 times reduction in computing time than the *H* homogenization method without compromising simulation accuracy and hence enables AC loss simulation in the transformer with over ten thousand turns. The same method can be applied to other large-scale HTS applications.

Upon exploiting the measured $I_c(B, \theta)$ characteristic of SuperPower HTS wire at 65 K by flipping the coil orientation, the maximum ac loss reduction reached 51 W (1.32%) in the transformer windings by orienting all the coils in their optimal orientations. To achieve the efficiency target of the designed 6.5 MVA/25 kV traction transformer, flux diverters of different geometries were introduced at the ends of both the LV and HV windings. Compared to the 3.90 kW AC loss without flux diverters, the total AC loss of the transformer was reduced to 1.80 kW with square flux diverters at 65 K. Through increasing the cross-section of the flux diverters, an extra 150 W reduction in AC loss was obtained with this square shape. Furthermore, an additional AC loss reduction of 37 W was achieved upon taking the $I_c(B, \theta)$ asymmetry into consideration, further increasing the efficiency of the transformer. It is worth emphasizing that these levels of loss reduction are achieved at 65 K. While translated to room temperature, the combined impact of asymmetric critical current and flux diverters provides over 5.6 kW energy saving for the power system on the Chinese Fuxing high-speed train. Furthermore, we demonstrate that this substantial saving can be achieved through a simple, cost-neutral procedure (flipping the coils) that is unique to the high temperature superconducting windings being used. This hitherto unrecognized optimization is of great value to anyone building an HTS transformer.

Most importantly of all, the article is a documentation of the design process of a replacement transformer for the Chinese high-speed rail network. As such a real-life endeavor, it has broad value and importance to the field of transportation electrification.

REFERENCES

[1] S. W. Schwenerly, B. W. McConnel, J. A. Demko, A. Fadnek, J. Hsu, F. A. List, M. S. Walker, D. W. Hazelton, F. S. Murray, and J. A. Rice, "Performance of a 1-MVA HTS demonstration transformer," *IEEE Trans. Appl. Supercond.*, vol. 9, no. 2, pp. 680-684, Jun. 1999.

[2] M. Leghissa, B. Gromoll, J. Rieger, M. Oomen, H. W. Neumüller, R. Schlosser, H. Schmidt, W. Knorr, M. Meinert, and U. Henning, "Development and application of superconducting transformers," *Phy. C: Supercond. its Appl.*, vol. 372-376, pp. 1688-1693, Aug. 2002.

[3] R. Schlosser, H. Schmidt, M. Leghissa, and M. Meinert, "Development of high-temperature superconducting transformers for railway applications," *IEEE Trans. Appl. Supercond.*, vol. 13, no. 2, pp. 2325-2330, Jun. 2003.

[4] M. Meinert, M. Leghissa, R. Schlosser, and H. Schmidt, "System test of a 1-MVA-HTS-transformer connected to a converter-fed drive for rail vehicles," *IEEE Trans. Appl. Supercond.*, vol. 13, no. 2, pp. 2348-2351, Jun. 2003.

[5] M. Iwakuma, H. Hayashi, H. Okamoto, A. Tomioka, M. Konno, T. Saito, Y. Iijima, Y. Suzuki, S. Yoshida, and Y. Yamada, "Development of REBCO superconducting power transformers in Japan," *Phy. C: Supercond. its Appl.*, vol. 469, no. 15-20, pp. 1726-1732, Oct. 2009.

[6] W. Song, Z. Jiang, M. Staines, R. A. Badcock, and J. Zhang, "Design of a single-phase 6.5 MVA/25 kV superconducting traction transformer for the Chinese Fuxing high-speed train," *Int. J. Electr. Power Energy Syst.*, vol. 119, Jun. 2020, Art. no. 105956.

[7] K. Funaki, M. Iwakuma, K. Kajikawa, M. Hara, J. Suehiro, T. Ito, Y. Takata, T. Bohno, S.Nose, M. Konno, Y. Yagi, H. Maruyama, T. Ogata, S. Yoshida, K. Ohashi, H. Kimura, and K. Tsutsumi, "Development of a 22 kV/6.9 kV single-phase model for a 3 MVA HTS power transformer," *IEEE Trans. Appl. Supercond.*, vol. 11, no. 1, pp. 1578-1581, Mar. 2001.

[8] Y. Wang, J. Han, X. Zhao, H. Li, Y. Guan, Q. Bao, L. Xiao, L. Lin, Z. Zhu, and S. Dai, "Development of a 45 kVA single-phase model HTS transformer," *IEEE Trans. Appl. Supercond.*, vol. 16, no. 2, pp. 1477-1480, Jun. 2006.

[9] Y. Wang, X. Zhao, J. Han, H. Li, Y. Guan, Q. Bao, L. Xiao, L. Lin, X. Xu, and N. Song, "Development of a 630 kVA three-phase HTS transformer with amorphous alloy cores," *IEEE Trans. Appl. Supercond.*, vol. 17, no. 2, pp. 2051-2054, Jul. 2007.

[10] M. Iwakuma, K. Sakaki, A. Tomioka, T. Miyayama, M. Konno, H. Hayashi, H. Okamoto, Y. Gosho, T. Eguchi, S. Yoshida, Y. Suzuki, H. Hirai, Y. Iijima, T. Saitoh, T. Izumi, and Y. Shiohara, "Development of a 3 Φ-66/6.9 kV-2 MVA REBCO Superconducting Transformer," *IEEE Trans. Appl. Supercond.*, vol. 25, no. 3, Jun. 2015, Art. no. 5500206.

[11] N. Glasson, M. Staines, N. Allpress, M. Pannu, J. Tanchon, E. Pardo, R. Badcock, and R. Buckley "Test results and conclusions from a 1 MVA superconducting transformer featuring 2G HTS Roebel cable," *IEEE Trans. Appl. Supercond.*, vol. 27, no. 4, Jun. 2017, Art. no. 5500205.

[12] D. Hu, Z. Li, Z. Hong, and Z. Jin, "Development of a single-phase 330kVA HTS transformer using GdBCO tapes," *Phy. C: Supercond. its Appl.*, vol. 539, pp. 8-12, Aug. 2017.

[13] M. Yazdani-Asrami, M. Staines, G. Sidorov, M. Davies, J. Bailey, N. Allpress, N. Glasson and S. A. Gholamian, "Fault current limiting HTS transformer with extended fault withstand time," *Supercond. Sci. Technol.*, vol. 32, no. 3, Jan. 2019, Art. no. 035006.

[14] A. Moradnouri, M. Vakilian, A. Hekmati, and M. Fardmanesh, "HTS transformer windings design using distributive ratios for minimization of short circuit forces," *J. Supercond. Nov. Magn.*, vol. 32, no. 2, pp. 151-158, 2019.

[15] W. Song, Z. Jiang, M. Staines, S. Wimbush, R. Badcock, and J. Fang, "AC loss calculation on a 6.5 MVA/25 kV HTS traction transformer with hybrid winding structure," *IEEE Trans. Appl. Supercond.*, vol. 30, no. 4, Jun. 2020, Art. no. 5500405.

[16] W. Pi, T. Wang, H. Zhang, Y. Yang, and Y. Wang, "Design and simulation of a 120 kVA single-phase HTS transformer," *IEEE Trans. Appl. Supercond.*, vol. 30, no. 4, Jun. 2020, Art. no. 5500305.

[17] M. P. Oomen, M. Leghissa, N. Proelss, and H. W. Neumueller, "Transposed-cable coil & saddle coils of HTS for rotating machines: Test results at 30 K," *IEEE Trans. Appl. Supercond.*, vol. 19, no. 3, pp. 1633-1638, Jun. 2009.

[18] M. Oomen, W. Herkert, D. Bayer, P. Kummeth, W. Nick, and T Arndt, "Manufacturing and test of 2G-HTS coils for rotating machines: Challenges, conductor requirements, realization," *Phy. C: Supercond. its Appl.*, vol. 482, pp. 111-118, Nov. 2012.

[19] K. S. Haran, S. Kalsi, T. Arndt, H. Karmaker, R. Badcock, B. Buckley, T. Haugan, M. Izumi, D. Loder, and J. W. Bray, "High power density superconducting rotating machines-development status and technology roadmap," *Supercond. Sci. Technol.*, vol. 30, no. 12, Nov. 2017, Art. no. 123002.

[20] J. H. Kim, C. J. Hyeon, H. L. Quach, S. H. Chae, Y. S. Chae, J. H. Moon, C. J. Boo, Y. S. Yoon, J. Lee, H. Jeon, S. Han, Y. G. Kim, H. Lee, and H. M. Kim, "Design, analysis, and fabrication of salient field-pole for a 1-kW-class HTS rotating machine," *Cryogenics*, vol. 97, pp. 126-132, Jan. 2019.

[21] G. Messina, M. Yazdani-Asrami, F. Marignetti, and A. D. Corte, "Characterization of HTS coils for superconducting rotating electric machine applications: challenges, material selection, winding process, and testing," *IEEE Trans. Appl. Supercond.*, vol. 31, no. 2, Mar. 2021, Art. no. 5200310.

[22] H. Thomas, A. Marian, A. Chervyakov, S. Stückrad, D. Salmieri, and C. Rubbia, "Superconducting transmission lines – Sustainable electric energy transfer with higher public acceptance," *Renew. Sustainable Energy Rev.*, vol. 55, pp. 59-72, Mar. 2016.

[23] W. H. Fietz, M. J. Wolf, A. Preuss, R. Heller, and K. P. Weiss, "High-Current HTS Cables: Status and Actual Development," *IEEE Trans. Appl. Supercond.*, vol. 26, no. 4, Jun. 2016, Art. no. 4800705.

[24] V. Altov, N. N. Balashov, P. N. Degtyarenko, S. Ivanov, and V.V. Zheltov, "Optimization of three- and single-phase AC HTS cables design by numerical simulation," *IEEE Trans. Appl. Supercond.*, vol. 27, no. 4, Jun. 2017, Art. no. 4801606.

[25] S. J. Lee, M. Park, I. K. Yu, Y. Won, and Y. Kwak, "Recent status and progress on HTS cables for AC and DC power transmission in Korea," *IEEE Trans. Appl. Supercond.*, vol. 28, no. 4, Jun. 2018, Art. no. 5401205.

[26] W. Schmidt, B. Gamble, H. P. Kraemer, D. Madura, A. Otto, and W. Romanosky, "Design and test of current limiting modules using YBCO-coated conductors," *Supercond. Sci. Technol.*, vol. 23, no. 1, Dec. 2009, Art. no. 014024.

[27] G. Didier, C. Bonnard, T. Lubin, and J. Lévêque, "Comparison between inductive and resistive SFCL in terms of current limitation and power system transient stability," *Electr. Pow. Syst. Res.*, vol. 125, pp. 150-158, Aug. 2015.

[28] N. Hayakawa, Y. Maeno, and H. Kojima, "Fault current limitation coordination in electric power grid with superconducting fault current limiters," *IEEE Trans. Appl. Supercond.*, vol. 28, no. 4, Jun. 2018, Art, no. 5602304.

[29] S. Dai, T. Ma, C. Xue, L. Zhao, Y. Huang, L. Hu, B. Wang, T. Zhang, X. Xu, L. Cai, and H. Chen, "Development and test of a 220 kV/1.5 kA resistive type superconducting fault current limiter," *Phy. C: Supercond. its Appl.*, vol. 565, Oct. 2019, Art. no. 1253501.

[30] M. Yazdani-Asrami, M. Staines, G. Sidorov, and A. Eicher, "Heat transfer and recovery performance enhancement of metal and superconducting tapes under high current pulses for improving fault current-limiting behavior of HTS transformers," *Supercond. Sci. Technol*., vol. 33, no. 9, Aug. 2020, Art. no. 095014.

[31] W. Song, X. Pei, J. Xi and X. Zeng, "A novel helical superconducting fault current limiter for electric propulsion aircraft," *IEEE Trans. Transp. Electrification*, vol. 7, no. 1, pp. 276-286, Mar. 2021.

[32] W. Song, X. Pei, H. Alafnan, J. Xi, and Z. Liu, "Experimental and simulation study of resistive helical HTS fault current limiters: quench and recovery characteristics," *IEEE Trans. Appl. Supercond.*, vol. 31, no. 5, Aug. 2021, Art. no. 5601106.

[33] N. M. Strickland, and S. C. Wimbush, "The magnetic-field dependence of critical current: what we really need to know," *IEEE Trans. Appl. Supercond.*, vol. 27, no. 4, Jun. 2017, Art. no. 8000505.

[34] S. C. Wimbush and N. M. Strickland, "A public database of high-temperature superconductor critical current data," *IEEE Trans. Appl. Supercond.*, vol. 27, no. 4, Jun. 2017, Art. no. 8000105.

[35] The Robinson Research Institute of Victoria University of Wellington, Wellington, New Zealand., "High-temperature superconducting wire critical current database," 2021. [Online]. Available: http://htsdb.wimbush.eu/

[36] L. Ren, S. Guo, G. Chen, L. Su, Y. Xu, J. Shi, and L. Chen, "Experimental research on critical current behavior of various commercial HTS tapes," *IEEE Trans. Appl. Supercond.*, vol. 30, no. 4, Jun. 2020, Art. no. 6601006.

[37] M. D. Ainslie, C. W. Bumby, Z. Jiang, R. Toyomoto, and N. Amemiya, "Numerical modelling of dynamic resistance in high-temperature superconducting coated-conductor wires," *Supercond. Sci. Technol.*, vol. 31, no. 7, Jun. 2018, Art. no. 074003.

[38] Z. Hong, W. Li, Y. Chen, F. Gömöry, L. Frolek, M. Zhang, and J. Sheng, "Design optimization of superconducting coils based on asymmetrical characteristics of REBCO tapes," *Phy. C: Supercond. its Appl.*, vol. 550, pp. 74-77, Jul. 2018.

[39] Z. Jiang, N. Endo, S. C. Wimbush, J. C. Brooks, W. Song, R. A. Badcock, D. Miyagi, and M. Tsuda, "Exploiting asymmetric wire critical current for the reduction of AC loss in HTS coil windings," *J. Phys. Commun.*, vol. 3, no. 9, Sep. 2019, Art. no. 095017.

[40] Y. Sun, J. Fang, A. E. Pantoja, R. A. Badcock, N. J. Long, and Z. Jiang, "Role of asymmetric critical current on magnetization loss characteristics of (RE)$Ba_2Cu_3O_{7-d}$ coated conductors at various temperatures," *J. Appl. Phys.*, vol. 130, no. 8, Aug. 2021, Art. no. 083902.

[41] Z. Jiang, W. Song, X. Pei, J. Fang, R. A. Badcock, and S.C. Wimbush, "15% reduction in AC loss of a 3-phase 1 MVA HTS transformer by exploiting asymmetric conductor critical current," *J. Phys. Commun.*, vol. 5, no. 2, Feb. 2021, Art. no. 025003.

[42] E. Pardo, J. Šouc, and M. Vojenčiak, "AC loss measurement and simulation of a coated conductor pancake coil with ferromagnetic parts," *Supercond. Sci. Technol.*, vol. 22, no. 7, Jun. 2009, Art. no. 075007.

[43] M. D. Ainslie, W. Yuan, and T. J. Flack, "Numerical analysis of AC loss reduction in HTS superconducting coils using magnetic materials to divert flux," *IEEE Trans. Appl. Supercond.*, vol. 23, no. 3, Jun. 2013, Art. no. 4700104.

[44] M. D. Ainslie, D. Hu, J. Zou, and D. A. Cardwell, "Simulating the in-field AC and DC performance of high-temperature superconducting coils," *IEEE Trans. Appl. Supercond.*, vol. 25, no. 3, Jun. 2015, Art. no. 4602305.

[45] X. Deng, Y. Tang, L. Ren, S. Shen, Y. Xu, J. Shi, and J. Li, "The effect of flux diverters on energy storage capacity and heat losses in a HTS SMES," *IEEE Trans. Appl. Supercond.*, vol. 24, no. 3, Jun. 2014, Art. no. 2284428.

[46] G. Liu, G. Zhang, L. Jing, L. Ai, Y. Hui, W. Li, and L. Qi, "Study on the AC loss reduction of REBCO double pancake coil," *IEEE Trans. Appl. Supercond.*, vol. 28, no. 8, Dec. 2018, Art. no. 8201606.

[47] S. You, M. Staines, G. Sidorov, D. Miyagi, and Z. Jiang, "AC loss measurement and simulation in a REBCO coil assembly utilising low-loss magnetic flux diverters," *Supercond. Sci. Technol.*, vol. 33, no. 11, Sep. 2020, Art. no. 115011.

[48] Y. Xing, J. Jin, B. Du, R. Sun, X. Chen, F. Li, Z. Chen, L. Ba, H. You, and Z. Jiang, "Influence of flux diverter on magnetic field distribution for HTS transformer windings," *IEEE Trans. Appl. Supercond.*, vol. 26, no. 7, Oct. 2016, Art. no. 5501305.

[49] S. Wu, J. Fang, L. Fang, A. Zhang, Y. Wang, and Y. Wu, "The influence of flux diverter structures on the AC loss of HTS transformer windings," *IEEE Trans. Appl. Supercond.*, vol. 29, no. 2, Mar. 2019, Art. no. 5501105.

[50] W. Song, Z. Jiang, X. Zhang, M. Staines, R. A. Badcock, J. Fang, Y. Sogabe, and N. Amemiya, "AC loss simulation in a HTS 3-Phase 1 MVA transformer using H formulation." *Cryogenics*, vol. 94, pp. 14-21, Sep. 2018.

[51] Z. Hong, A. M. Campbell, and T. A. Coombs, "Numerical solution of critical state in superconductivity by finite element software," *Supercond. Sci. Technol.*, vol. 19, no. 12, pp. 1246-1252, Oct. 2006.

[52] R. Brambilla, F. Grilli, and L. Martini, "Development of an edge-element model for AC loss computation of high-temperature superconductors," *Supercond. Sci. Technol.*, vol. 20, no. 1, pp. 16-24, Nov. 2006.

[53] F. Grilli, R. Brambilla, and L. Martini, "Modeling high-temperature superconducting tapes by means of edge finite elements," *IEEE Trans. Appl. Supercond.*, vol. 17, no. 2, pp. 3155-3158, Jun. 2007.

[54] H. Zhang, M. Zhang, and W. Yuan, "An efficient 3D finite element method model based on the T–A formulation for superconducting coated conductors," *Supercond. Sci. Technol.*, vol. 30, no. 2, Dec. 2016, Art. no. 024005.

[55] E. Berrospe-Juarez, F. Trillaud, V. Zermeño, and F. Grilli, "Advanced electromagnetic modeling of large-scale high-temperature superconductor systems based on H and T-A formulations," *Supercond. Sci. Technol.*, vol. 34, no. 4, Feb. 2021, Art. no. 044002.

[56] J. R. Clem, J. H. Claassen, and Y. Mawatari, "AC losses in a finite Z stack using an anisotropic homogeneous-medium approximation," *Supercond. Sci. Technol.*, vol. 20, no. 12, pp. 1130-1139, Sep. 2007.

[57] V. M. R. Zermeno, A. B. Abrahamsen, N. Mijatovic, B. B. Jensen, and M. P. Serensen, "Calculation of alternating current losses in stacks and coils made of second generation high temperature superconducting tapes for large scale applications," *J. Appl. Phys.*, vol. 114. no. 17, Nov. 2013, Art. no. 173901.

[58] E. Berrospe-Juarez, V. M. R. Zermeño, F. Trillaud, and F. Grilli, "Real-time simulation of large-scale HTS systems: multi-scale and homogeneous models using the T–A formulation," *Supercond. Sci. Technol.*, vol. 32, no. 6, Apr. 2019, Art. no. 065003.

[59] 2G HTS Wire Specification. [Online]. Available: https://www.superpower-inc.com/specification.aspx.

[60] N. Amemiya, S. Murasawa, N. Banno, K. Miyamoto, "Numerical modelings of superconducting wires for AC loss calculations," *Phy. C: Supercond. its Appl.*, vol. 310, no. 1-4, pp. 16-29, Dec. 1998.

[61] N. Nibbio, S. Stavrev, and B. Dutoit, “Finite element method simulation of AC loss in HTS tapes with B-dependent E-J power law,” *IEEE Trans. Appl. Supercond.*, vol. 11, no. 1, pp. 2631-2634, Mar. 2001.

[62] H. Ueda, Y. Imaichi, T. Wang, A. Ishiyama, S. Noguchi, S. Iwai, H. Miyazaki, T. Tosaka, S. Nomura, T. Kurusu, S. Urayama, and H. Fukuyama, "Numerical simulation on magnetic field generated by screening current in 10-T-class REBCO coil," *IEEE Trans. Appl. Supercond.*, vol. 26, no. 4, Jun. 2016.

[63] S. Matsutomo, S. Noguchi, and H. Yamashita, “Adaptive mesh generation method utilizing magnetic flux lines in two-dimensional finite element analysis,” *IEEE Trans. on Magn.*, vol. 48, no. 2, pp. 527-530, Feb. 2012.

[64] M. Zhang, M. Chudy, W. Wang, Y. Chen, Z. Huang, Z. Zhong, W. Yuan, J. Kvitkovic, S. V. Pamidi, and T. A. Coombs, “AC loss estimation of HTS armature windings for electric machines," *IEEE Trans. Appl. Supercond.*, vol. 23, no. 3, Jun. 2013, Art no. 5900604.

[65] Y. Yan, T. Qu, and F. Grilli, “Numerical modeling of AC loss in HTS coated conductors and Roebel cable using T-A formulation and comparison with H formulation," *IEEE Access*, vol. 9, pp. 49649-49659, Mar. 2021.

[66] S. You, S. S. Kalsi, M. D. Ainslie, R. A. Badcock, N. J. Long, and Z. Jiang, “Simulation of AC loss in the armature windings of a 100 kW all-HTS motor with various (RE)BCO conductor considerations,” *IEEE Access*, vol. 9, pp. 130968-130980, Sep. 2021.

[67] F. Huber, W. Song, M. Zhang, and F. Grill, “The T-A formulation: an efficient approach to model the macroscopic electromagnetic behaviour of HTS coated conductor applications,” *Supercond. Sci. Technol.*, vol. 35, no. 4, Mar. 2022, Art. no. 043003.

[68] E. Pardo, M. Staines, Z. Jiang, and N. Glasson, “AC loss modelling and measurement of superconducting transformers with coated-conductor Roebel-cable in low-voltage winding,” *Supercond. Sci. Technol.*, vol. 28, no. 11, Oct. 2015, Art. 114008.

[69] Y. B. Kim, C. F. Hempstead, and A. R. Strnad, “Critical persistent currents in hard superconductors,” *Phys. Rev. Lett.*, vol. 9. no. 7, pp. 306-309, Oct. 1962.

[70] S. Terzieva, M. Vojenčiak, E. Pardo, F. Grilli, A. Drechsler, A. Kling, A. Kudymow, F. Gömöry, and W. Goldacker, “Transport and magnetization ac losses of ROEBEL assembled coated conductor cables: measurements and calculations,” *Supercond. Sci. Technol.*, vol. 23, no. 1, Dec. 2009, Art. 014023.

[71] Z. Jiang, R. Badcock, N. Long, M. Staines, K. Thakur, L. Lakshmi, A. Wright, K. Hamilton, G. Sidorov, R. Buckley, N. Amemiya, and A. Caplin, “Transport AC loss characteristics of a nine strand YBCO Roebel cable,” *Supercond. Sci. Technol.*, vol. 23, no. 2, Jan. 2010, Art. 025028.

[72] M. Staines, M Yazdani-Asrami, N. Glasson, N. Allpress, L. Jolliffe, E. Pardo, “Cooling systems for HTS transformers: impact of cost, overload, and fault current performance expectations,” *Proc. 2nd Int. Workshop Cooling Syst. HTS Appl. (IWC-HTS)*, 2017.